Bilinear Discrete-Time Modeling and Stability Analysis of the Digitally Controlled Dual Active Bridge Converter

Ling Shi, Wanjun Lei, *Member, IEEE*, Zhuoqiang Li, Jun Huang, Yao Cui, and Yue Wang, *Member, IEEE*

***Abstract*—Dual active bridge (DAB) converters have been widely used in distributed power systems and energy storage equipment. However, the inherent nonlinearity of the DAB converters can cause stability problem, such as output voltage oscillation. In this paper, the dynamic behavior and stability of a digitally controlled DAB converter with a closed-loop controller are studied. First, to accurately study the nonlinear dynamics and stability in a DAB converter, a bilinear discrete-time model considering the output capacitor equivalent series resistance (ESR) and the digital control delay in circuit is established. Based on the model, the nonlinear dynamic characteristic and stability of the DAB converter versus the control parameter are studied. Furthermore, extensive analyses are performed to study the effect of the transformer leakage inductance and the output capacitor ESR on the stability boundaries of the control parameter. The accuracy of the model and the theoretical analyses are validated by simulation and experimental results. The proposed model of the digitally controlled DAB converter can accurately predict the stability boundaries, which can be effectively applied to the design of the system parameters and guarantee stable operation of the converter.**

***Index Terms*—Dual active bridge (DAB) converter, discrete-time modeling, nonlinear dynamics, stability analysis.**

I. Introduction

POWER electronic converters continue to evolve as an indispensable part in many electronic circuits. However, nonlinear dynamics such as period doubling bifurcation [1], [2], Hopf bifurcation [3], [4], and chaos [1], [2], [4] are affluent in these converters. In practice, as these abnormal operations increase the switching stress of the converter and affect the transmission efficiency, a better understanding of the system under all possible operating conditions is needed to help provide useful guidelines for a reliable design, thereby keeping the bifurcations far enough from the operating conditions in parameter space and improving its performance.

Manuscript received July 1, 2016; revised September 19, 2016; accepted November 28, 2016. Date of publication December 19, 2016; date of current version June 23, 2017. Recommended for publication by Associate Editor M. Ordonez. *(Corresponding author: Wanjun Lei.)*

The authors are with the State Key Laboratory of Electrical Insulation and Power Equipment, Shaanxi Key Laboratory of Smart Grid, School of Electrical Engineering, Xi'an Jiaotong University, Xi'an 710049, China (e-mail: lingshi@stu.xjtu.edu.cn; leiwanjun@mail.xjtu.edu.cn; lizhuoqiang20@stu.xjtu.edu.cn; hjxjtu@stu.xjtu.edu.cn; cuiyao1618@stu.xjtu.edu.cn; davidwangyue@mail.xjtu.edu.cn).

Color versions of one or more of the figures in this paper are available online at http://ieeexplore.ieee.org.

Digital Object Identifier 10.1109/TPEL.2016.2640659

DC–DC converters are some of the most widely used circuits in power electronics and many researchers have devoted to the dynamic behavior in dc–dc converters over the past several decades [5]–[10]. Recently, the development of renewable energy storage [11], plug-in hybrid electric vehicles [12], uninterruptible power supply systems [13], and smart grids [14] has increased the popularity of the bidirectional dc–dc converters. Compared with other bidirectional dc–dc converters, the dual active bridge (DAB) converters have been taken more attention because of its advantages on galvanic isolation, zero-voltage switching (ZVS), high power density, high efficiency, and symmetric structure [15], [16]. Thus, this converter has been extensively analyzed and design methodology [17], control strategies [18], [19], and modulation strategies [20] have been proposed. However, due to the existence of switching nonlinearity and control delay [21], the complex dynamics in the DAB converters, which can deteriorate the performance and bring instability, have not been studied in the existing literature.

To study the dynamics in a DAB converter, an appropriate model should be developed. Generally, the dynamics in converters can be analyzed based on the state-space averaged model or the discrete-time model [4], [22], [23]. The averaged model has each circuit variable averaged within one switching period. Thus, this approach does not consider the switching details and is only useful to detect the slow-scale dynamics of the system. However, the discrete-time model can predict the state variables at one sampling time based on previous samples. As a result, the discrete-time model can predict both the slow- and fast-scale dynamics of the system.

Establishing a conventional averaged model in a DAB converter is not appropriate as the leakage inductance current is alternating and current ripple cannot be negligible. Thus, in [24], a simplified reduced-order averaged model is established by neglecting the conduction loss and the output capacitor ESR. This model averages the inductance current in each state interval. In [25] and [26], the small-signal model of the DAB converter is developed by averaging and perturbing the output current. The three models above are all derived by averaging the steady-state current and thus neglect the inductance current dynamic. In [27], a generalized averaged model, which uses several terms in the Fourier series of state variables, is established. If high accuracy of this model is required, the order of the system will be evidently increased. Many

researchers have also made much effort to establish discrete-time models for DAB converters. In [28], a discrete-time averaged model averaging the value of the output voltage over half switching period is obtained. This model can be updated every half switching period and is suitable for half period control. In [29], a discrete-time small-signal model without considering the output capacitor ESR is developed. In [30] and [31], due to the symmetry of the leakage inductance current and the output voltage in steady state, the discrete-time models for half period control are established in a half switching period. In [32], a discrete-time model is established to accurately describe the instability of a DAB converter. And analysis is performed to study the effects of the output capacitor ESR and the control parameter on the stability of the system.

In this paper, to optimize and simplify the calculation process in [32], a bilinear approximation method of the matrix exponential proposed in [33] is added and the process of calculating the steady-state point is improved. This model is called the bilinear discrete-time model. The bilinear discrete-time model takes into account the output capacitor ESR and considers the digital control delay and sample-and-hold process. Using the bilinear discrete-time model established in this paper, the bifurcation point when the system becomes unstable is accurately predicted in terms of the bifurcation diagrams and the eigenvalues of the Jacobian matrix. Furthermore, extensive analyses are performed to study the effects of the leakage inductance and the output capacitor ESR on the stability boundaries of the control parameter. Then, a comparison between the bilinear discrete-time model and three other models is made under the same conditions and the simulation results prove that the bilinear discrete-time model is more accurate.

The rest of the paper is organized as follows. In Section II, the system description of a digitally controlled DAB converter is given. In Section III, the bilinear discrete-time model is established to describe the system. Then, in Section IV, with the bilinear discrete-time model, the stabilities of the DAB converter versus several parameters are analyzed and the margins of stability curve are obtained. Also, a comparison with three other models is made to prove the accuracy of the proposed model. In Section V, simulation and experimental results are shown based on the numerical parameters to verify the theoretical analysis. Finally, conclusions are provided in Section VI.

II. System Description

The DAB converter is a topology with the advantages of decreased number of devices, high power density, high power efficiency resulting from ZVS, and low cost. The DAB converter can be used in systems that require galvanic isolation and bidirectional power flow ability between two dc buses with different voltage levels.

The schematic of a digitally controlled DAB converter is shown in Fig. 1, including a power stage and a digital controller. The power stage consists of a high-frequency transformer with 1: *n* turn ratios and two H-bridges. The high-frequency transformer provides the required galvanic isolation and voltage matching between two voltage buses. The transformer leakage inductance

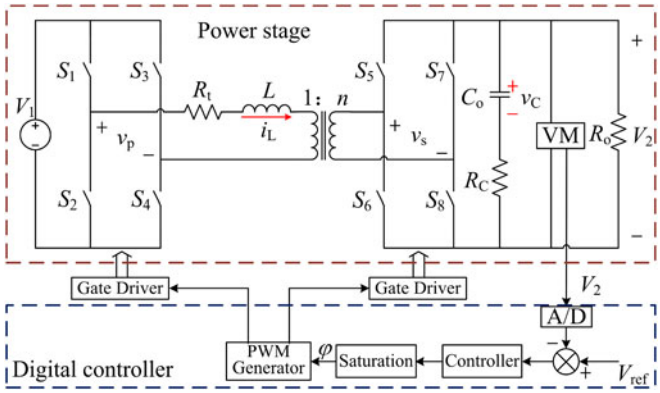

Fig. 1. Diagram of a digitally controlled DAB converter.

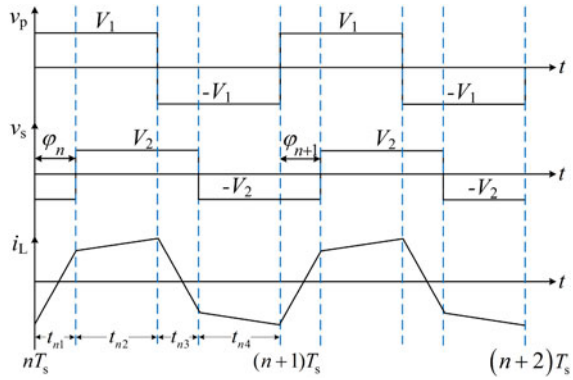

Fig. 2. Operation waveforms in the steady state.

L serves as the instantaneous energy storage device. Take the power flow from V_1 side to V_2 side as an example. V_1 is the input dc voltage and V_2 is the output dc voltage. R_t is the sum of the on-resistors of switches, the transformer winding resistances, and the line resistance. C_o is the output capacitor. R_C is the output capacitor ESR. The converter operates at a fixed switching frequency f_s.

The control strategy of a DAB converter can be classified in the following methods:

1) the single-phase-shift (SPS) control;
2) the extended-phase-shift (EPS) control;
3) the dual-phase-shift (DPS) control;
4) the triple-phase-shift (TPS) control.

For simplicity, this paper only analyzes the SPS control, which is also the most widely used control strategy for DAB converters [11], [16], [34]. In the SPS control, the cross-connected switch pairs in both H-bridges are switched in turn to generate phase-shifted square wave voltages v_p and v_s with 50% duty ratio to primary and secondary sides of the transformer. A phase shift angle φ between v_p and v_s can be adjusted to control the power flow. The operation waveforms in steady state when φ is positive are shown in Fig. 2 and the power flows from the V_1 side to the V_2 side. There are four intervals in one switching period and the converter operates symmetrically in each half period, with two state intervals.

A digital controller which consists of output-voltage feedback and one-step-delay control is adopted in this system. The output

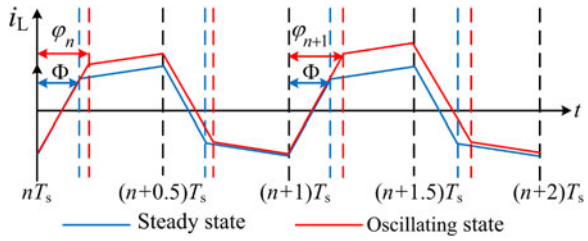

Fig. 3. Operation waveforms in the steady state and the oscillating state.

voltage V_2 is sampled by the controller at the beginning of each switching period and is compared with the voltage reference. Under the control of the controller and the saturator element, the phase shift φ is calculated and loaded at the beginning of the next switching period. The saturator element controls the range of φ, which is from 0 to $\pi/2$.

If one parameter in circuit is inappropriate, the phase shift angle φ may keep oscillating and the system may lose stability such as in Fig. 3. The blue solid line is the steady-state inductor current waveform, and Φ is the steady-state value of phase shift. The red solid line is the oscillating inductor current waveform and φ_{n+1}, φ_{n+2} are the oscillating phase shift. It can be observed from the red solid line that the inductor current is not symmetrical about half switching period and may have much wider amplitude if the oscillation is more intense, which can cause transformer saturation and audible noise. Also, the inductor current oscillation results in the output voltage oscillation and decreases the quality of power supply. All of these can have undesirable impact on device stress and are generally not preferred. So establishing an appropriate model and studying the dynamics and stability of the digitally controlled DAB converter is necessary.

III. Bilinear Discrete-Time Modeling

A. Derivation of the System State Equations

The model in this paper is derived by assuming that transistor switching transients are negligible. The input capacitance is usually relatively large. Therefore, the dynamics of the input capacitor are not considered in this paper. To proceed with the bilinear discrete-time modeling of the converter, the system state equations are derived first. Corresponding to the subintervals $t_{n1} - t_{n4}$ in Fig. 2, the system exhibits four possible states during a switching period given by

Subinterval t_{n1} : S_1, S_4, S_6, S_7 are ON; S_2, S_3, S_5, S_8 are OFF;

Subinterval t_{n2} : S_1, S_4, S_5, S_8 are ON; S_2, S_3, S_6, S_7 are OFF;

Subinterval t_{n3} : S_2, S_3, S_5, S_8 are ON; S_1, S_4, S_6, S_7 are OFF;

Subinterval t_{n4} : S_2, S_3, S_6, S_7 are ON, S_1, S_4, S_5, S_8 are OFF.

Equivalent circuits during each subintervals $t_{n1} - t_{n4}$ are drawn in Fig. 4. The system state equations of the converter in the four subintervals take the form as

$$\dot{x}(t) = A_i x(t) + B_i V_1 \tag{1}$$

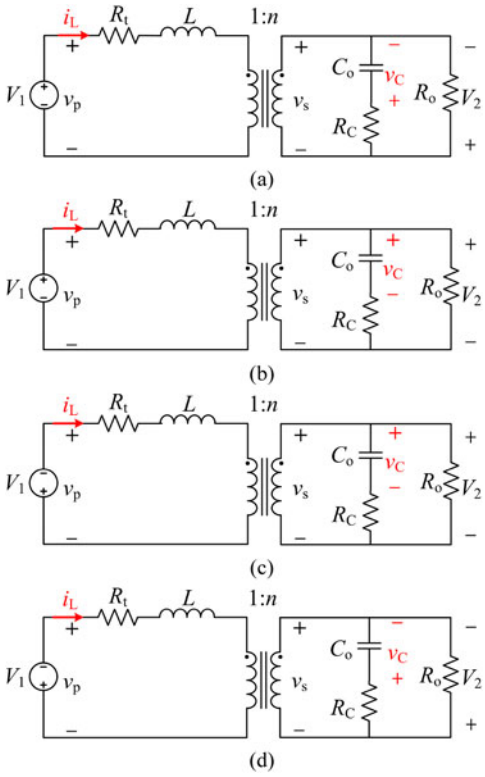

Fig. 4. Equivalent circuits during subintervals t_{n1}, t_{n2}, t_{n3}, t_{n4}. (a) Subinterval t_{n1}. (b) Subinterval t_{n2}. (c) Subinterval t_{n3}. (d) Subinterval t_{n4}.

where $x(t) = [\, i_L \;\; v_C \,]^T$ is a state vector, A_i and B_i are system matrices and vectors, V_1 is input voltage source, and $i = 1, 2, 3, 4$ considers the four subintervals in one switching period.

If the output capacitor ESR is considered during the modeling, the matrices A_i and vectors B_i are expressed as follows:

$$A_1 = A_4 = \begin{bmatrix} -\dfrac{n^2 R_t + R_o R_C / (R_o + R_C)}{n^2 L} & \dfrac{R_o}{nL(R_C + R_o)} \\ -\dfrac{R_o}{nC_o(R_o + R_C)} & -\dfrac{1}{C_o(R_o + R_C)} \end{bmatrix}$$

$$A_2 = A_3 = \begin{bmatrix} -\dfrac{n^2 R_t + R_o R_C / (R_o + R_C)}{n^2 L} & -\dfrac{R_o}{nL(R_C + R_o)} \\ \dfrac{R_o}{nC_o(R_o + R_C)} & -\dfrac{1}{C_o(R_o + R_C)} \end{bmatrix} \tag{2}$$

$$B_1 = B_2 = \begin{bmatrix} \dfrac{1}{L} & 0 \end{bmatrix}^T, \quad B_3 = B_4 = \begin{bmatrix} -\dfrac{1}{L} & 0 \end{bmatrix}^T. \tag{3}$$

Then if the output capacitor ESR R_C is not considered ($R_C = 0\ \Omega$), the matrices A_i are expressed in a rather simple way in

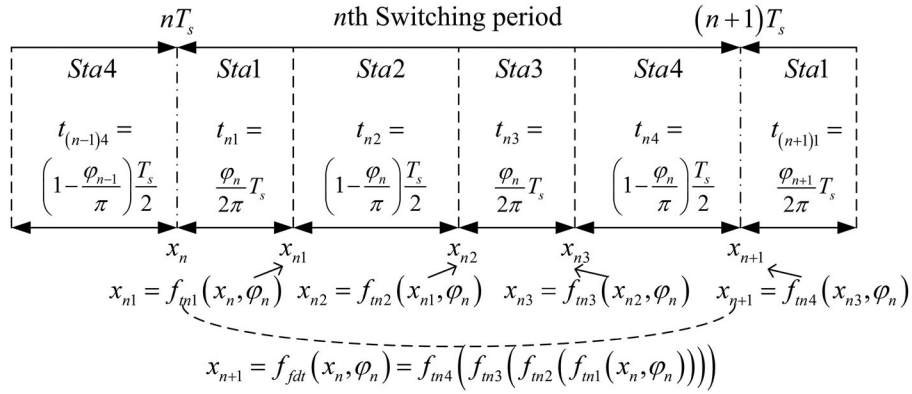

Fig. 5. State variables iteration relationship.

(4) and the vectors B_i are as same as (3).

$$A_1 = A_4 = \begin{bmatrix} -\dfrac{R_t}{L} & \dfrac{1}{Ln} \\ -\dfrac{1}{nC_o} & -\dfrac{1}{C_oR_o} \end{bmatrix},$$
$$A_2 = A_3 = \begin{bmatrix} -\dfrac{R_t}{L} & -\dfrac{1}{Ln} \\ \dfrac{1}{nC_o} & -\dfrac{1}{C_oR_o} \end{bmatrix}. \quad (4)$$

B. Derivation of the Bilinear Discrete-Time Modeling

To obtain the map model of the digitally controlled DAB converter, the most widely used discrete-time modeling of switching dc–dc converters is adopted. The discrete-time model is derived from regular sampling of the state variables of the continuous-time dynamics without making quasi-static approximation such as small ripple and high switching frequency. Modeling of this system can be divided into two parts, including the part of the power stage and the digital control system as shown in Fig. 1. During the modeling, the two cases that whether the ESR R_C is considered are discussed. However, the modeling processes of the power stage in the two cases are exactly the same. So the difference will just be discussed separately in the modeling of the digital control system.

The power converter has four switching states in one switching cycle, as shown in Fig. 2. Let the initial conditions of x and V_2 at the beginnings of the nth and the $(n+1)$th switching cycles be denoted as $x_n = [i_{Ln}\, V_{cn}]^T$, V_{2n} and $x_{n+1} = [i_{L(n+1)}\, V_{c(n+1)}]^T$, $V_{2(n+1)}$, respectively. A discrete-time model can be derived in each switching state by the state variables, which can be expressed as (5) and Fig. 5 illustrates the iteration relationship of the state variables in one switching period.

$$\begin{aligned} x_{n1} &= f_{n1}(x_n, \varphi_n) = e^{A_1 t_{n1}} x_n + \psi_1 V_1 \\ x_{n2} &= f_{n2}(x_{n1}, \varphi_n) = e^{A_2 t_{n2}} x_{n1} + \psi_2 V_1 \\ x_{n3} &= f_{n3}(x_{n2}, \varphi_n) = e^{A_3 t_{n3}} x_{n2} + \psi_3 V_1 \\ x_{n+1} &= f_{n4}(x_{n3}, \varphi_n) = e^{A_4 t_{n4}} x_{n3} + \psi_4 V_1 \end{aligned} \quad (5)$$

where

$$\begin{aligned} t_{n1} &= t_{n3} = \varphi_n/(2\cdot f_s \cdot \pi), \\ t_{n2} &= t_{n4} = 1/(2\cdot f_s) - \varphi_n/(2\cdot f_s \cdot \pi) \\ \psi_1 &= \int_0^{t_1} e^{A_1 t_{n1}} B_1 dt = A_1^{-1}(e^{A_1 t_{n1}} - I)B_1 \\ \psi_2 &= \int_0^{t_2} e^{A_2 t_{n2}} B_2 dt = A_2^{-1}(e^{A_2 t_{n2}} - I)B_2 \\ \psi_3 &= \int_0^{t_3} e^{A_3 t_{n3}} B_3 dt = A_3^{-1}(e^{A_3 t_{n3}} - I)B_3 \\ \psi_4 &= \int_0^{t_4} e^{A_4 t_{n4}} B_4 dt = A_4^{-1}(e^{A_4 t_{n4}} - I)B_4. \end{aligned} \quad (6)$$

Based on Fig. 5 and (5), the discrete-time model of the power stage in one switching cycle, denoted as f_{fdt}, can be written as

$$\begin{aligned} x_{n+1} &= f_{fdt}(x_n, \varphi_n) \\ &= f_{\mathrm{tn4}}(f_{\mathrm{tn3}}(f_{\mathrm{tn2}}(f_{\mathrm{tn1}}(x_n, \varphi_n)))) \\ &= e^{A_4 t_{n4}}\left\{e^{A_3 t_{n3}}\left[e^{A_2 t_{n2}}\left(e^{A_1 t_{n1}} x_n + \psi_1 V_1\right) + \psi_2 V_1\right]\right. \\ &\quad \left. + \ \psi_3 V_1\right\} + \psi_4 V_1 \\ &= F(\varphi_n)\, x_n + G(\varphi_n)\, V_1 \end{aligned} \quad (7)$$

where

$$\begin{aligned} F(\varphi_n) &= e^{A_4 t_{n4}} \cdot e^{A_3 t_{n3}} \cdot e^{A_2 t_{n2}} \cdot e^{A_1 t_{n1}}, \\ G(\varphi_n) &= e^{A_4 t_{n4}} \cdot e^{A_3 t_{n3}} \cdot e^{A_2 t_{n2}} \psi_1 + e^{A_4 t_{n4}} \cdot e^{A_3 t_{n3}} \cdot \psi_2 \\ &\quad + e^{A_4 t_{n4}} \cdot \psi_3 + \psi_4. \end{aligned} \quad (8)$$

So the discrete-time model of the power stage is obtained and can be expected highly accurate. However, the model involving matrix exponentials is too complex and difficult to use for control design. Conventionally, the model can be simplified by replacing the matrix exponentials by their first-order approximation, i.e.,

$$\begin{aligned} e^{A_1 t_{n1}} &= I + A_1 t_{n1},\ e^{A_2 t_{n2}} = I + A_2 t_{n2} \\ e^{A_3 t_{n3}} &= I + A_3 t_{n3},\ e^{A_4 t_{n4}} = I + A_4 t_{n4}. \end{aligned} \quad (9)$$

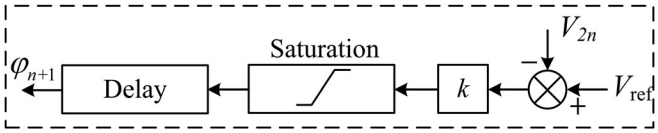

Fig. 6. Block diagram of a digital controller.

Then, an approximate conventional bilinear model is obtained and is in a much simpler form. Nevertheless, the approximation (9) requires that $\|A_1 t_{n1}\|$, $\|A_2 t_{n2}\|$, $\|A_3 t_{n3}\|$, and $\|A_4 t_{n4}\|$ be small simultaneously. Since these four conditions usually do not hold at the same time, the resulting model can be expected to have limited accuracy. Considering this, a bilinear approximation method of the matrix exponential [33] is used to approximate the matrix exponentials involved in (7) by expanding them around the steady-state operation phase shift, as

$$\begin{aligned} e^{A_1 t_{n1}} &= e^{A_1 T_\Phi} e^{A_1 (t_{n1} - T_\Phi)} \approx e^{A_1 T_\Phi} \left(I + A_1 \left(t_{n1} - T_\Phi\right)\right) \\ e^{A_2 t_{n2}} &= e^{A_2 (T_s/2 - T_\Phi)} e^{A_2 (t_{n2} - T_s/2 + T_\Phi)} \\ &\approx e^{A_2 (T_s/2 - T_\Phi)} \left(I + A_2 \left(t_{n2} - T_s/2 + T_\Phi\right)\right) \\ e^{A_3 t_{n3}} &= e^{A_3 T_\Phi} e^{A_3 (t_{n3} - T_\Phi)} \approx e^{A_3 T_\Phi} \left(I + A_3 \left(t_{n3} - T_\Phi\right)\right) \\ e^{A_4 t_{n4}} &= e^{A_4 (T_s/2 - T_\Phi)} e^{A_4 (t_{n4} - T_s/2 + T_\Phi)} \\ &\approx e^{A_4 (T_s/2 - T_\Phi)} \left(I + A_4 \left(t_{n4} - T_s/2 + T_\Phi\right)\right). \end{aligned} \quad (10)$$

where $T_\Phi = \Phi/2\pi f_s$ and Φ is the steady-state phase shift. Note that the remaining matrix exponentials in (10) do not involve the control variables and hence can be computed before-hand as constant matrices. Then an approximate but accurate bilinear discrete-time model is obtained in (11) by substituting (10) into (7).

$$x_{b(n+1)} = F_b\left(\varphi_n\right) x_{\text{bn}} + G_b\left(\varphi_n\right) V_1. \quad (11)$$

The detailed block diagram of the closed-loop digital controller is shown in Fig. 6. For simplicity, take a proportional controller as an example and *k* is the controller proportional coefficient. The controller modeled here considers one step control delay. First, the controller samples the output voltage V_2 periodically at the starting time $t = nT_s$ of each switching cycle and then compares it with the reference output voltage V_{ref} to obtain the voltage error. Furthermore, the error goes through *k* and the saturation to get a phase shift angle φ. The controller updates the phase shift angle command φ at the starting time $t = (n+1)T_s$ of the next switching cycle. The discrete-time model of the digital control system can be expressed as (12), from which it can be observed that this discrete-time model can deal with the time delay accurately. If a more complicated control method is considered, the digital controller modeling process can be modified but the analysis method in the following steps can also be used.

$$\begin{aligned} \varphi_{n+1} &= k\left(V_{\text{ref}n} - V_{2n}\right) \\ &= k\left(V_{\text{ref}n} - V_{\text{ex}} x_{\text{bn}}\right) \ \varphi_{n+1} \in [0, \pi/2]. \end{aligned} \quad (12)$$

If the output capacitor ESR R_C is not considered, the sampling voltage V_{2n} is equal to the iteration variable V_{cn}. So V_{ex} can be written as

$$V_{\text{ex}} = \begin{bmatrix} 0 & 1 \end{bmatrix}. \quad (13)$$

If the output capacitor ESR R_C is considered, the sampling voltage V_{2n} is relevant to both the iteration variable V_{cn} and the inductance current i_{Ln} at the time of $t = nT_s$, and V_{ex} is expressed as

$$V_{\text{ex}} = \begin{bmatrix} -R_o R_C / \left(R_o + R_C\right) & R_o / \left(R_o + R_C\right) \end{bmatrix}. \quad (14)$$

Finally, the bilinear discrete-time model composed of (11) and (12) can be rearranged and expressed in the formation of (15). This model can be expected to be highly accurate and to preserve all the essential characteristics of the converter.

$$\begin{cases} i_{bL(n+1)} = \begin{bmatrix} 1 & 0 \end{bmatrix} x_{b(n+1)} \\ v_{bC(n+1)} = \begin{bmatrix} 0 & 1 \end{bmatrix} x_{b(n+1)} \\ \varphi_{(n+1)} = k\left(V_{\text{ref}n} - R_o / \left(R_o + R_C\right) \cdot \begin{bmatrix} -R_C & 1 \end{bmatrix} x_{\text{bn}}\right) \\ \varphi_{(n+1)} \in [0, \pi/2] \end{cases}. \quad (15)$$

IV. Stability Analysis of the DAB Converter

The system parameters have great effects on the stability of the whole system. If the system parameters are not suitable, the inductor current and the output voltage may appear obvious oscillation phenomenon. As the system parameters are varied, how a system changes from its fundamental operation to bifurcation behavior is a question that needs to be figured out.

In this section, first, two bifurcation diagrams are drawn to make a comparison between the two cases whether to consider the output capacitor ESR R_C. Then, the bifurcation type when R_C is considered is determined with the help of the eigenvalues of the corresponding Jacobian matrix. Furthermore, the stability boundary at different values of the controller proportional coefficient *k* and R_C is demonstrated. Meanwhile, while considering R_C, the stability boundary at different values of *k* and the transformer leakage inductance *L* is also demonstrated and some conclusions are made at last.

A. Bifurcation Diagram Analysis

The bifurcation diagram is a powerful tool to investigate the nonlinear phenomenon. In a bifurcation diagram, a periodic steady state of a system is represented as a single point or several points that equal to the periodicity of the system for a fixed parameter, while the chaotic state of the system is represented as numerous points because chaos means period infinity and does not fall at the same position. Therefore, in such a bifurcation diagram, the behavior change of a system is clearly shown when a parameter is varied. From the theoretical point of view, any circuit parameter can work as a bifurcation parameter.

In this section, the proportional coefficient *k* of the controller is selected as the bifurcation parameter. The parameter *k* is varied from 0.01 to 8 with a step of 0.01, while other parameters are kept the same as illustrated in Table I.

Equations (5) and (12) can be used in MATLAB to obtain all the points of the inductor current i_L at each switching time. The

TABLE I
SYSTEM PARAMETERS

Parameters	Value	Parameters	Value
V_1	30 V	R_o	12.5 Ω
L	35.49 μH	f_s	20 kHz
R_t	0.38 Ω	n	1
C	455 μF	V_{ref}	30 V
R_C	0.45 Ω	k	0.1–8

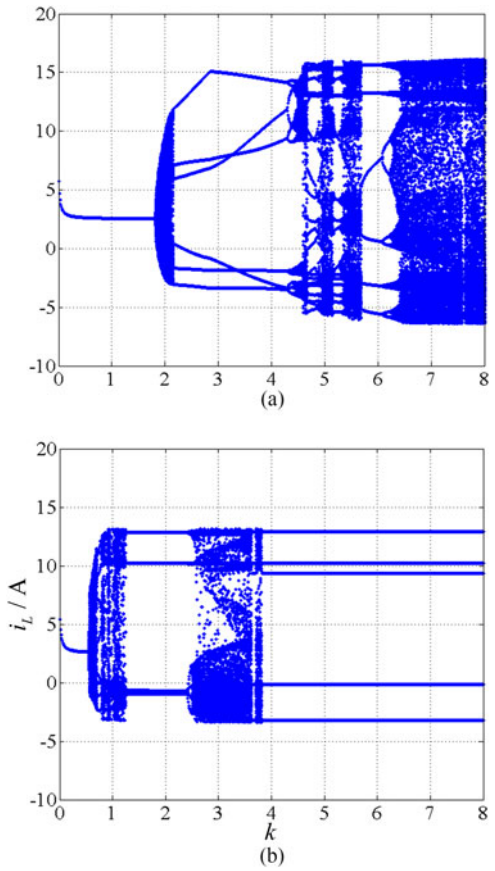

Fig. 7. Bifurcation diagram for inductor current using k as the bifurcation parameter. (a) $R_C = 0\ \Omega$. (b) $R_C = 0.45\ \Omega$.

points at half of each switching period are chosen to draw the bifurcation diagrams as shown in Fig. 7(a) and (b).

Fig. 7(a) is the case that R_C is not considered. The system jumps out of the stable period-1 state when the parameter k is more than 1.81. Fig. 7(b) is the case that R_C is considered and equals to the value 0.45 Ω as shown in Table I. The system jumps out of the stable period-1 state when the parameter k is more than 0.55. In addition to this, with the increasing of k, variation trend of the inductor current i_L is obviously different. In Fig. 7(a), the inductor current i_L enters a state of chaos when k is big enough. However, in Fig. 7(b), i_L does not enter a state of chaos when k is bigger than 3.86. Therefore, when the stability of a DAB converter is analyzed, it is important to consider the output capacitor ESR R_C, which will help us accurately predict the bifurcation point and development tendency.

B. Jacobian Matrix Analysis

The stability of the system and the bifurcation type can be analyzed with the help of the eigenvalues of the corresponding Jacobian matrix. If the eigenvalues have at least one absolute value greater than 1, the system will be unstable. Considering the analysis above, in the following sections, we will only discuss the case that considers the output capacitor ESR R_C in the system. The Jacobian matrix can be obtained as shown in (16) by taking the partial derivatives of (15). Finally, the eigenvalues $\lambda_{J1}, \lambda_{J2}, \lambda_{J3}$ are the solutions of (17).

$$J(I_L, V_C, \Phi) = \begin{bmatrix} \frac{\partial i_{bL(n+1)}}{\partial i_{bLn}} & \frac{\partial i_{bL(n+1)}}{\partial v_{bCn}} & \frac{\partial i_{bL(n+1)}}{\partial \varphi_{bn}} \\ \frac{\partial v_{bC(n+1)}}{\partial i_{bLn}} & \frac{\partial v_{bC(n+1)}}{\partial v_{bCn}} & \frac{\partial v_{bC(n+1)}}{\partial \varphi_{bn}} \\ \frac{\partial \varphi_{b(n+1)}}{\partial i_{bLn}} & \frac{\partial \varphi_{b(n+1)}}{\partial v_{bCn}} & \frac{\partial \varphi_{b(n+1)}}{\partial \varphi_{bn}} \end{bmatrix} \tag{16}$$

$$\det(\lambda I - J(I_L, V_C, \Phi)) = 0. \tag{17}$$

It should be mentioned that the stability analyses require the Jacobian matrix expressed in (16) to be estimated in the operation point (I_L, V_C, Φ). $X = [I_L\ V_C]^T$ is the constant state vector at the time $t = nT_s$. Usually, this operating point is in steady state and the state variables are symmetric. Thus, an inverting quasi-identity matrix I_{HC} can be defined to describe the relationship of x_n and x_{n2} in steady state as follows:

$$x_{n2} = I_{HC} x_n \tag{18}$$

where $I_{HC} = [-1, 0; 0, 1]$ defines the symmetry of the state variables.

From Fig. 5, the discrete-time model of x_n and x_{n2} can be written as

$$\begin{aligned} x_{n2} &= f_{tn2}(f_{tn1}(x_n, \varphi_n)) \\ &= e^{A_2 t_{n2}}\left(e^{A_1 t_{n1}} x_n + \psi_1 V_1\right) + \psi_2 V_1. \end{aligned} \tag{19}$$

Capitals are used to represent the steady-state values of the subintervals $t_{n1} - t_{n2}$ and exponential matrices in (6), as in (20) and (21). Then the solution for the operating point (I_L, V_C) can be obtained by solving (18) and (19). The result is given in (23). Then, the constant phase shift Φ is obtained by (24).

$$\begin{aligned} T_{n1} &= \Phi/(2 \cdot f_s \cdot \pi), \\ T_{n2} &= 1/(2 \cdot f_s) - \Phi/(2 \cdot f_s \cdot \pi) \end{aligned} \tag{20}$$

$$\Psi_1 = A_1^{-1}(e^{A_1 T_{n1}} - I)B_1 V_1,$$

$$\Psi_2 = A_2^{-1}(e^{A_2 T_{n2}} - I)B_2 V_1 \tag{21}$$

$$e^{A_i T_{ni}} = I + A_i T_{ni} + 0.5(A_i T_{ni})^2 \quad (i = 1,\ 2) \tag{22}$$

$$\begin{aligned} X = &\left(I_{HC} - e^{A_2 T_{n2}} e^{A_1 T_{n1}}\right)^{-1} \\ &\times \left(e^{A_2 T_{n2}} \Psi_1 V_1 + \Psi_2 V_1\right) V_1 \end{aligned} \tag{23}$$

$$\Phi = k(V_{ref} - R_o/(R_o + R_C)[-R_C\ 1]X). \tag{24}$$

Stability and bifurcation analysis of the system will be carried out with the control parameter k as an example. The process of

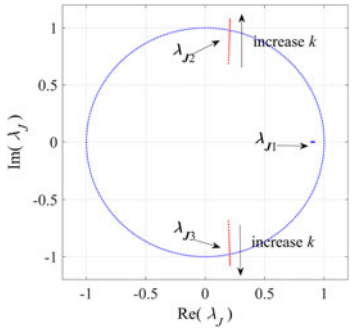

Fig. 8. Trajectory of eigenvalues for various values of *k*.

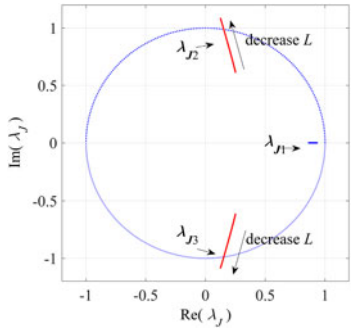

Fig. 9. Trajectory of eigenvalues for various values of *L*.

TABLE II
EIGENVALUES AT $L = 35.49\ \mu$H, $R_C = 0.45\ \Omega$ FOR VARIOUS VALUES OF *k*

k	Eigenvalues λ_{J1}-λ_{J3}	Absolute value	Remarks
0.51	$0.8987, 0.2041 \pm 0.9319$	0.8987, 0.9540	Stable
0.53	$0.8975, 0.2047 \pm 0.9519$	0.8975, 0.9737	Stable
0.55	$0.8964, 0.2052 \pm 0.9715$	0.8964, 0.9929	Stable
0.57	$0.8953, 0.2058 \pm 0.9908$	0.8953, 1.012	Unstable
0.59	$0.8943, 0.2063 \pm 1.010$	0.8943, 1.031	Unstable

TABLE III
EIGENVALUES AT $k = 0.4$, $R_C = 0.45\ \Omega$ FOR VARIOUS VALUES OF *L*

L/μH	Eigenvalues λ_{J1}-λ_{J3}	Absolute value	Remarks
26.5	$0.8848, 0.1587 \pm 0.9661$	0.8789, 0.9790	Stable
26.0	$0.8834, 0.1562 \pm 0.9752$	0.8774, 0.9876	Stable
25.5	$0.8819, 0.1536 \pm 0.9843$	0.8758, 0.9962	Stable
25.0	$0.8805, 0.1511 \pm 0.9934$	0.8804, 1.005	Unstable
24.5	$0.8789, 0.1485 \pm 1.0003$	0.8789, 1.011	Unstable

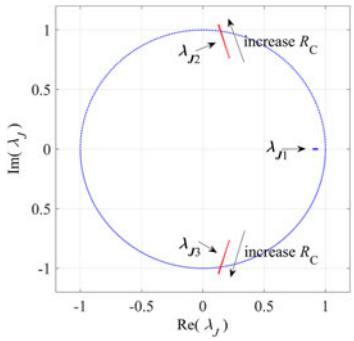

Fig. 10. Trajectory of eigenvalues for various values of R_C.

calculating eigenvalues to detect the border of the stability and instability can be summarized as follows: First for a given *k*, the steady-state phase shift angle Φ is calculated by substituting (23) into (24). Calculation of Φ involves a transcendent equation and it can be solved with the Newton iteration method. Then, the calculated phase shift angle Φ is substituted in (23) to calculate the steady-state vector $X = [\, I_L \;\; V_C \,]$. The calculated steady-state operation point (I_L, V_C, Φ) is obtained and substituted in (16) to calculate the Jacobian matrix. Finally, eigenvalues are calculated through (17). The border between stability and instability will be obtained by gradually increasing *k* to calculate the eigenvalues. The process is performed in MATLAB, as it allows matrix exponential computation and symbolic derivation. To speed up the calculation process, matrix exponential in (21) can be replaced by (22).

When $L = 35.49\ \mu$H and $R_C = 0.45\ \Omega$, the control parameter *k* is swept from 0.31 to 0.65 with a step of 0.02. The trajectory of the eigenvalues around the unit circle is shown in Fig. 8. Meanwhile, the eigenvalues around the border of the unit circle are presented in Table II. From the three eigenvalues, it can be remarked that two conjugate eigenvalues vary with *k,* while the third one remains almost unchanged. Two conjugate ones exceed the unit circle when *k* is greater than 0.55, so the system exhibits Hopf bifurcation. A Hopf bifurcation is a local bifurcation in which a fixed point of a dynamical system loses stability, as a pair of complex conjugate eigenvalues of a continuous-time system cross the complex plane imaginary axis or a pair of complex conjugate eigenvalues of a discrete-time system cross the unit cycle [10], [35].

In this paper, the system is a discrete-time system and a pair of conjugate eigenvalues crosses the unit cycle when the parameters are not chosen appropriately. So the system exhibits Hopf bifurcation and low-frequency oscillations appear in the waveforms.

In order to further illustrate that the choices of the system parameters have great effect on the stability of the system, the leakage inductor *L* and the output capacitor ESR R_C are taken as the bifurcation parameters. First, keep the control parameter *k* equal to 0.4 and R_C equal to 0.45 Ω, and let *L* sweep from 20 to 50 μH with steps of 0.5 μH. The trajectory of eigenvalues around the unit circle is shown in Fig. 9. The eigenvalues around the border are presented in Table III. From the three eigenvalues, it can be remarked that two conjugate eigenvalues vary with *L* while the third one remains almost unchanged. It is the conjugate ones that exceed the unit circle when *L* decreases. Thus, the system exhibits Hopf bifurcation when *L* is less than 25.5 μH. Then, keep *k* equal to 0.4 and *L* equal to 35.49 mH, and let R_C sweep from 0.4 to 0.8 Ω with steps of 0.02 Ω. The trajectory of eigenvalues around the unit circle is shown in Fig. 10. The eigenvalues around the border are presented in Table IV. From the three eigenvalues, it can be remarked that two conjugate eigenvalues vary with R_C while the third one remains almost

TABLE IV
EIGENVALUES AT $k = 0.4$, $L = 35.49$ MH FOR VARIOUS VALUES OF R_C

R_C/Ω	Eigenvalues λ_{J1}-λ_{J3}	Absolute value	Remarks
0.66	0.9254, 0.1527 ± 0.9641	0.9254, 0.9762	Stable
0.68	0.9268, 0.1490 ± 0.9762	0.9268, 0.9875	Stable
0.70	0.9282, 0.1453 ± 0.9879	0.9282, 0.9985	Stable
0.72	0.9294, 0.1418 ± 0.9992	0.8804, 1.009	Unstable
0.74	0.9307, 0.1383 ± 1.010	0.8789, 1.020	Unstable

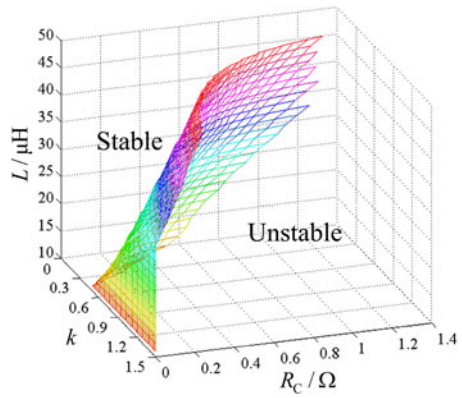

Fig. 11. Trajectory of eigenvalues for various values of *k*.

unchanged. It is the conjugate ones that exceed the unit circle when R_C increases. Thus, the system exhibits Hopf bifurcation when R_C is greater than 0.7 Ω.

Considering all above, the following summaries are made.

1) For lower values of *k* or R_C or higher values of *L*, two conjugate eigenvalues are located within the unit circle indicating the fixed point is a stable focus.
2) As *k* or R_C increases or *L* decreases, two conjugate eigenvalues get close to the unit circle and at a critical value, the two conjugate ones crosses the cycle, which implies an unstable focus.

C. Margin of Stability Curve

In the industry, the usual acceptable operation state is period-1 operation state, at which any bifurcations are avoided. If there is a Hopf bifurcation growing up in the system, the system will suddenly operate at a long-period limit cycle. The output voltage and inductor current will have much wider amplitude, which have undesirable impact on device stresses and are generally not preferred. In practice, bifurcations can affect the transfer efficiency and switching stress of the converters. Therefore, it is necessary to draw a bifurcation boundary that can be important for practical design to avoid the occurrence of such undesirable bifurcations.

In our study of the stability of the DAB converters above, it is discovered that the output capacitor ESR R_C and the leakage inductance *L* have greater influences on the system than any other parameters in the circuit. Therefore, the critical values of *k* at which the bifurcations occur are most dependent on the values of R_C and *L*. Thus, the stability boundary of *k*, R_C, and *L* in three-dimension is shown in Fig. 11. In order to clearly

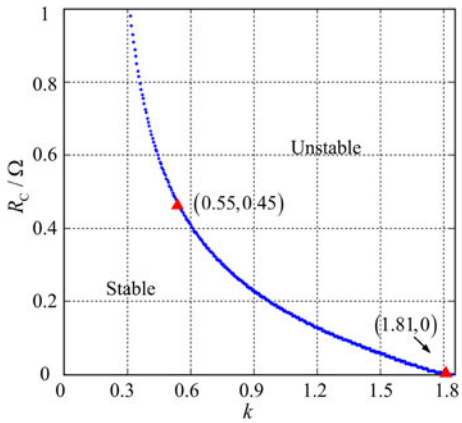

Fig. 12. Trajectory of eigenvalues for various values of *L*.

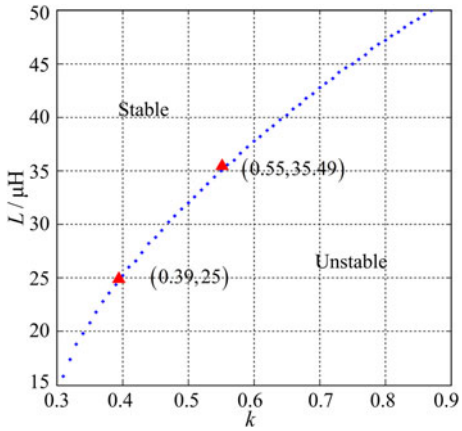

Fig. 13. Trajectory of eigenvalues for various values of R_C.

observe the effect of the value of *L* and R_C on critical value of *k*, the plane stability boundary of *k* and R_C when $L = 35.49$ μH and the plane stability boundary of *k* and *L* when $R_C = 0.45$ Ω are respectively shown in Figs. 12 and 13.

Then, the following observations and summaries are made.

1) From Fig. 11, it can be observed that if the value of R_C is low and the value of *L* is high, the stability range of *k* will be extended greatly.
2) Observed from Fig. 12, when $R_C = 0\,\Omega$, the critical value of *k* is equal to 1.81. When $R_C = 0.45\ \Omega$, the critical value of *k* is equal to 0.55. They are consistent with the observations from Fig. 7.
3) Observed from Fig. 12, R_C has great effect on the stability of the system, as the critical value of *k* is expanded significantly when R_C is decreased. This phenomenon points out that it is quite necessary to consider R_C when we design parameters for a DAB converter in practice.
4) It can be observed from Fig. 13 that *L* also has great effect on the stability of the system, as the critical value of *k* is expanded significantly when *L* is increased. However, the value of *L* cannot be very large when considering the power transmission.

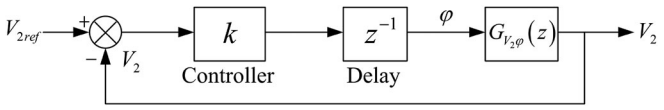

Fig. 14. Equivalent block diagram of the digitally controlled DAB converter.

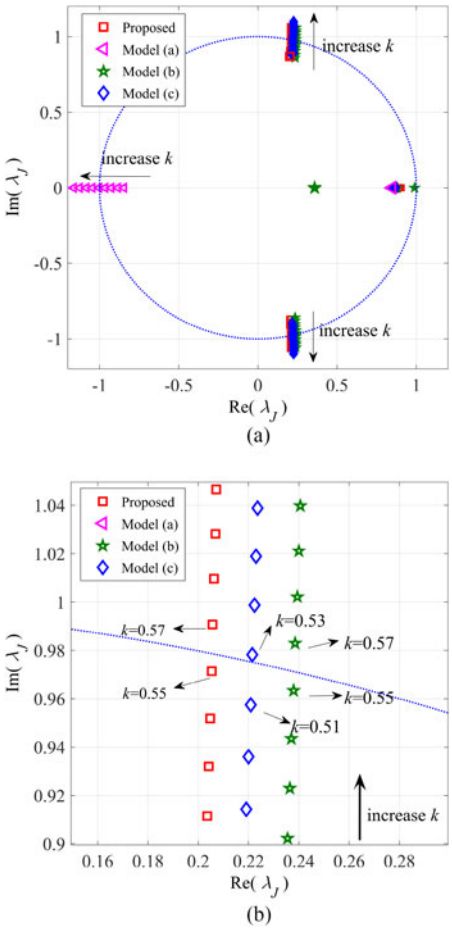

Fig. 15. Eigenvalues trajectory comparison when $L = 35.49\ \mu$H. (a) Trajectory of the eigenvalues. (b) Details of the eigenvalues.

D. Comparison With Different Models

For comparison, the eigenvalues predicted by three different models with the same operating parameters given in Table I are shown in Figs. 15 and 16.

1) Model (a) is presented in [25], which is derived from the steady-state output current with R_t and the output capacitor ESR R_C neglected. In this section, in order to make a better contrast, R_C is included in the s-transfer function from the phase shift to the output voltage $G_{V_2\varphi a}(s)$.
2) Model (b) is presented in [27], which is derived based on several terms in the Fourier series of state variables with the output capacitor ESR R_C included. Then an s-transfer function $G_{V_2\varphi b}(s)$ is derived directly.
3) Model (c) is the discrete-time small-signal model which is originally presented in [29] with the output capacitor ESR R_C neglected. In this section, the resonant transition intervals are neglected and R_C is included. Then, a z-transfer function $G_{V_2\varphi c}(z)$ can be obtained directly.

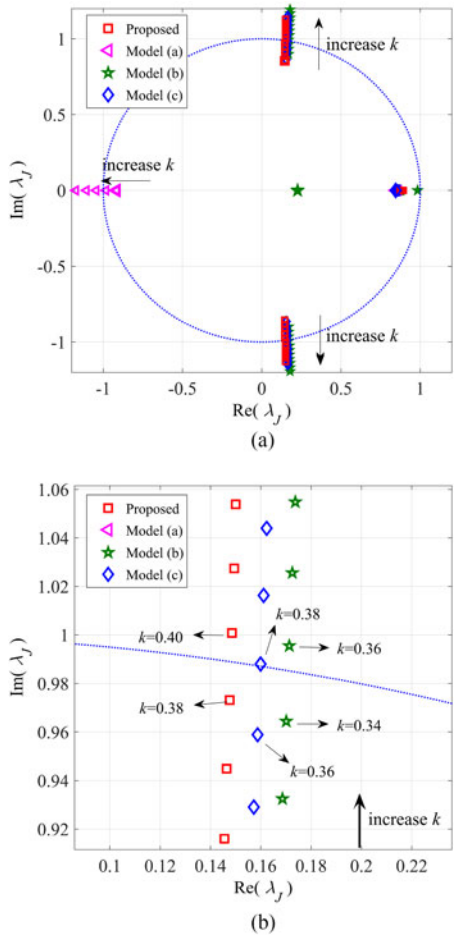

Fig. 16. Eigenvalues trajectory comparison when $L = 24.56\ \mu$H. (a) Trajectory of the eigenvalues. (b) Details of the eigenvalues.

To observe the position of the eigenvalues versus the unit circle, the z- transforms $G_{V_2\varphi a}(z)$ and $G_{V_2\varphi b}(z)$ of $G_{V_2\varphi a}(s)$ and $G_{V_2\varphi b}(s)$ should be developed first. Then, the closed-loop transfer function G_{cj} is derived from Fig. 14 and expressed in (25). The eigenvalues are the poles of (25).

$$G_{cj} = \frac{kz^{-1}G_{V_2\varphi j}(z)}{1 + kz^{-1}G_{V_2\varphi j}(z)}, j = a, b, c. \tag{25}$$

In order to compare the accuracy of predicting the critical value and the bifurcation type among the proposed model and the three selected models, we select two leakage inductances with different values and take the control parameter k as the bifurcation parameter. First, keep the leakage inductance value L equal to 35.49 μH and let k sweep from 0.45 to 0.65 with steps of 0.02. The eigenvalues trajectories of the four models around the unit circle are shown in Fig. 15.

Model (a) is found by averaging and perturbing the steady-state output current, that is, this model neglects the inductance current dynamic and $G_{ca}(z)$ has only two eigenvalues. In Fig. 15(a), one eigenvalue moves out of the unit cycle from $(-1, 0)$, while the other one remains practically unchanged. Thus, this model cannot predict the critical value and the bifurcation type precisely.

Model (b) uses the first coefficients of i_L as the state variable, so $G_{cb}(z)$ is a four-order equation and has four eigenvalues. Two of the eigenvalues stay inside the unit cycle and the other two conjugate eigenvalues exceed the unit circle when k increases. The system exhibits Hopf bifurcation when k is greater than 0.55.

The closed-loop transfer function $G_{cc}(z)$ of Model (c) is a three-order equation and has three eigenvalues. One eigenvalue stays inside the unit cycle and the other two conjugate eigenvalues exceed the unit circle when k increases. The system exhibits Hopf bifurcation when k is greater than 0.51.

The critical value of k in model (c) is less than the value 0.55, while the critical value of k in model (b) is equal to 0.55. And 0.55 is a critical value of k predicted by the proposed model in this paper. It seems that model (b) and the proposed model have the same ability to predict the critical value. Then, we can keep L equal to 24.56 μH and let k sweep from 0.30 to 0.50 with steps of 0.02. In Fig. 16, we can see that the critical values of k in model (b) and (c) are respectively 0.34 and 0.36, while the critical value of the proposed model is 0.38. In Section V, simulation result will prove that when L is equal to 35.49 or 24.56 μH, the system is stable until k is greater than 0.55 or 0.38. Thus, the proposed model gives the most accurate critical values of k.

V. Simulation and Experimental Verifications

In order to verify the theoretical analysis, simulations and experiments are carried out in this section.

A. Simulation Results

According to Fig. 1, the model of the system is built in MATLAB/Simulink. The "sample time" in the unit delay and sum module is set as T_s to simulate the time delay and the sampling and holding process.

First, when leakage inductance $L = 35.49$ μH, the simulation results when $k = 0.55$ and 0.57 are shown in Fig. 17. It can be observed that the system is stable when $k = 0.55$ and unstable when $k = 0.57$, which is consistent with the analysis of Fig. 8. The simulation results also prove that the system is stable when control parameter is inside the stability range in Fig. 12 and unstable in the opposite range.

Subsequently, in order to prove the effect of the leakage inductance value on the stability of the system, a transformer, of which leakage inductance value is 24.56 μH, is applied in the system. Then, the simulation results when $k = 0.38$ and 0.40 are shown in Fig. 18. It can be observed that the system is stable when $k = 0.38$ and unstable when $k = 0.40$, which is consistent with the analysis of Fig. 13.

Finally, from the simulation results, it can be concluded that when L is equal to 35.49 or 24.56 μH, the system is stable until k is greater than 0.55 or 0.38. The two critical values prove that the proposed model is more accurate than the three models listed in Section IV.

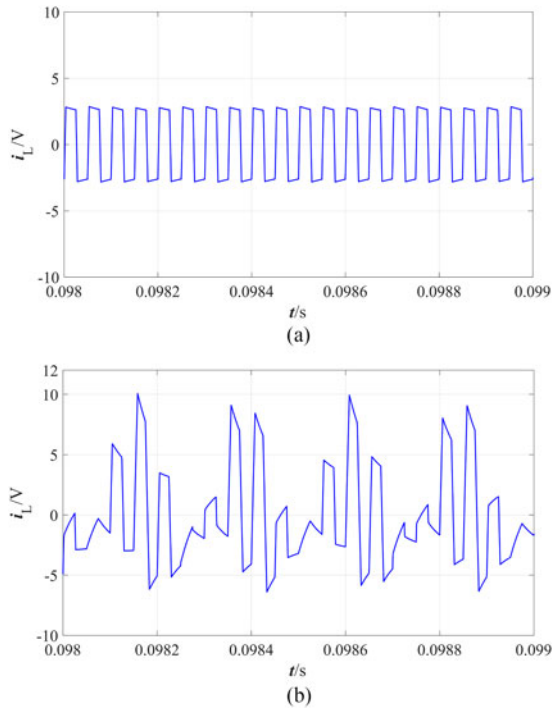

Fig. 17. Simulation results ($L = 35.49$ μH). (a) Inductor current when $k = 0.55$. (b) Inductor current when $k = 0.57$.

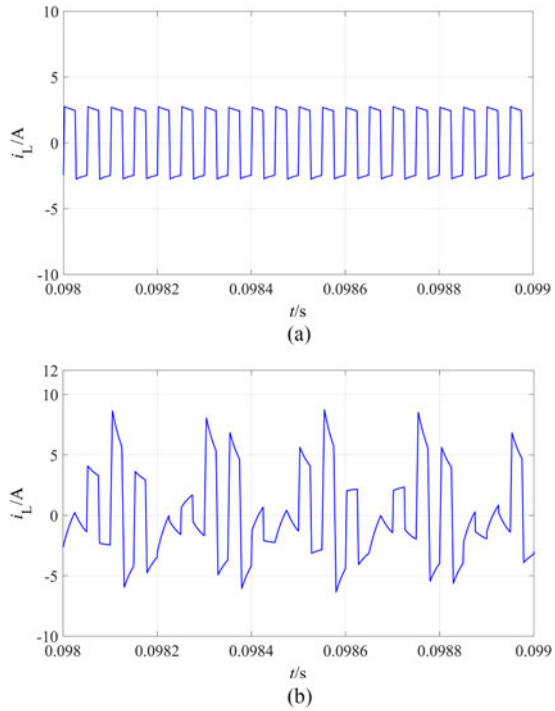

Fig. 18. Simulation results ($L = 24.56$ μH). (a) Inductor current when $k = 0.38$. (b) Inductor current when $k = 0.40$.

B. Experimental Verifications

Furthermore, an experimental platform with the same design parameter values used in the simulation is designed to validate the numerical and simulation results.

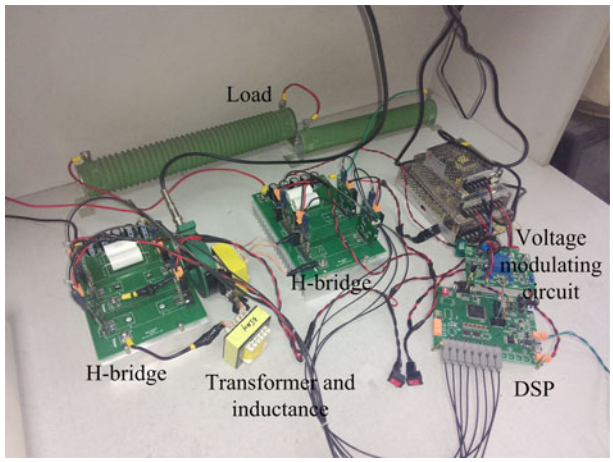

Fig. 19. Experimental platform.

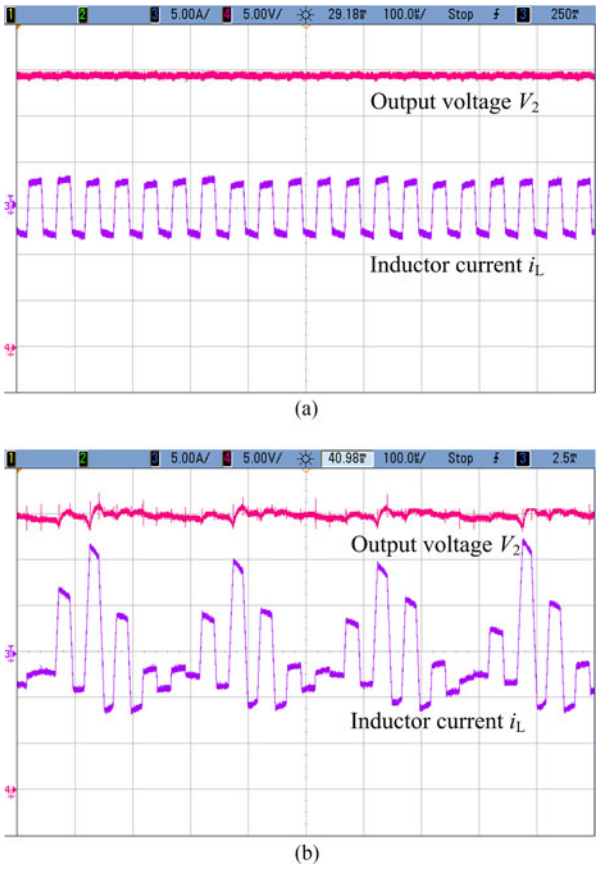

Fig. 20. Experimental results ($L = 35.49\ \mu$H). (a) Inductor current and output voltage when $k = 0.52$. (b) Inductor current and output voltage when $k = 0.5$.

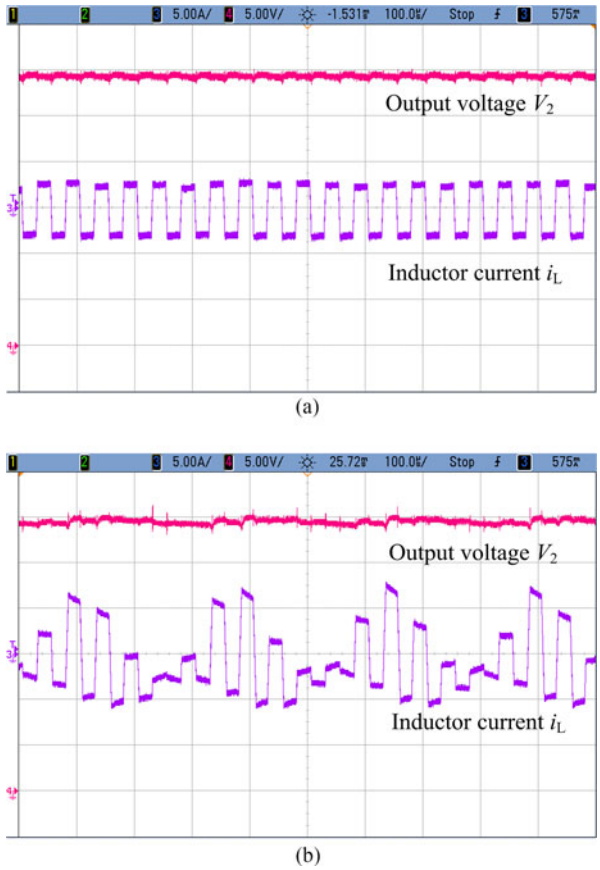

Fig. 21. Experimental results ($L = 24.56\ \mu$H). (a) Inductor current and output voltage when $k = 0.35$. (b) Inductor current and output voltage when $k = 0.40$.

Fig. 19 shows the platform. Power MOSFETs IXFK102N30P are applied to all the switches $S_1 - S_8$. The inductor and the transformer are made of litz wire and the capacitor is composed of five electrolytic capacitors. The output voltage is sensed and modulated by output voltage modulating circuit, where the voltage transducer LV25-P is used. Then, the output signal from the modulating circuit is given to the ADC channel of a TMS320F28335 DSP controller, where the voltage control algorithm is implemented. The bipolar 12 bit ADC in the DSP accepts a maximum of ± 3 V. For compatibility, the sensed output voltage is scaled down to less than $+3$ V using output voltage modulating circuit. The controller provides the necessary switching signals to the driver circuit. The driver circuit uses 1ED020I12-F driver ICs with the necessary circuit to provide isolation and amplification. Additionally, the Pearson wideband current monitor is used to measure the inductor current i_L, and the Agilent mixed-signal oscilloscope MSO7054A is employed to capture the measured waveforms.

The experimental results with the leakage inductance $L = 35.49\ \mu$H are shown in Fig. 20. When $k = 0.52$, the system is stable and there is no dc component in the inductor current i_L. When $k = 0.58$, the system is unstable and obvious oscillations appear in the output voltage V_2 and the inductor current i_L. The experimental results with the leakage inductance $L = 24.56\ \mu$H are shown in Fig. 21. The phenomena when $k = 0.35$ and $k = 0.40$ are the same as described above.

The experimentally measured waveforms clearly depict the same dynamical behavior as the analytical and simulation results, and it is obvious that there are low-frequency oscillations on the waveforms of the inductor current and the output voltage when k is greater than the critical value. Meanwhile, it is proved that the critical value of k is smaller when L is smaller. Furthermore, it is proved that when the system is unstable, the inductor current is not symmetrical about half switching period and has

much wider amplitude, which results in transformer saturation and noise. The oscillation of the output voltage also decreases the quality of power supply. All of these have undesirable impact on device stresses and are generally not preferred. Due to the impact of core loss, various parasitic elements, dead effect, and device model imperfections, the experimental waveforms do not have the same amplitude exactly as in simulation results, and there exists small deviations of k between experimental results and theoretical predictions. Then owing to the sampling error and noise jamming from adjacent modules, there are weak oscillations when $k = 0.52$ and $k = 0.35$.

VI. Conclusion

The nonlinear dynamics of a digitally controlled DAB converter is investigated in this paper. A bilinear discrete-time model is derived for the digitally controlled DAB converter with output voltage closed-loop control. The theoretical analyses indicate that Hopf bifurcation can take place when the system loses its stability with higher values of the control parameter or the output capacitor ESR or lower values of leakage inductance. Furthermore, it is also found that the output capacitor ESR and the leakage inductance can greatly affect the stability region of the control parameter. The critical value of the control parameter is expanded significantly when ESR is decreased or the leakage inductance is increased. It points out that it is quite necessary to consider the output capacitor ESR and the leakage inductance when designing parameters for a DAB converter in practice.

The above analysis in this paper is very helpful when analyzing the nonlinear dynamics of the digitally controlled DAB converters. Using the model in this paper, determining the effect of the circuit parameters on digitally controlled DAB converters is very practical and convenient. Meanwhile, the stability region provides useful guidelines for the appropriate design of the converter by keeping bifurcations far enough from the operating conditions in parameter space.

References

[1] J. H. B. Deane and D. C. Hamill, "Instability, subharmonics, and chaos in power electronic systems," *IEEE Trans. Power Electron.*, vol. 5, no. 3, pp. 260–268, Jul. 1990.

[2] D. C. Hamill, J. H. B. Deane, and D. J. Jefferies, "Modeling of chaotic DC-DC converters by iterated nonlinear mappings," *IEEE Trans. Power Electron.*, vol. 7, no. 1, pp. 25–36, Jan. 1992.

[3] W. Xuanlv, X. Guochun, and L. Bo, "Simplified discrete-time modeling for convenient stability prediction and digital control design," *IEEE Trans. Power Electron.*, vol. 28, no. 11, pp. 5333–5342, Nov. 2013.

[4] C. K. Tse and M. Di Bernardo, "Complex behavior in switching power converters," *Proc. IEEE*, vol. 90, no. 5, pp. 768–781, May 2002.

[5] P. Deivasundari, G. Uma, and S. Ashita, "Chaotic dynamics of a zero average dynamics controlled DC-DC Cuk converter," *IET Power Electron.*, vol. 7, pp. 289–298, 2014.

[6] X. Xiong, C. K. Tse, X. Ruan, and M. Huang, "Bifurcation analysis in dual-input buck converter in hybrid power system," in *Proc. 2013 IEEE Int. Symp. Circuits Syst.*, 2013, pp. 925–928.

[7] V. Moreno-Font, A. E. Aroudi, J. Calvente, R. Giral, and L. Benadero, "Dynamics and stability issues of a single-inductor dual-switching DC-DC converter," *IEEE Trans. Circuits Syst. I, Reg. Papers*, vol. 57, no. 2, pp. 415–426, Feb. 2010.

[8] D. Dong, C. K. Tse, and M. Xikui, "Symbolic analysis of switching systems: Application to bifurcation analysis of DC/DC switching converters," *IEEE Trans. Circuits Syst. I, Reg. Papers*, vol. 52, no. 8, pp. 1632–1643, Aug. 2005.

[9] X. Xiong, C. K. Tse, and X. Ruan, "Bifurcation analysis and experimental study of a multi-operating-mode photovoltaic-battery hybrid power system," *IEEE J. Emerging Sel. Topics Circuits Syst.*, vol. 5, no. 3, pp. 316–325, Sep. 2015.

[10] X. Xiong, C. K. Tse, and X. Ruan, "Bifurcation analysis of standalone photovoltaic-battery hybrid power system," *IEEE Trans. Circuits Syst. I, Reg. Papers*, vol. 60, no. 5, pp. 1354–1365, May 2013.

[11] S. Inoue and H. Akagi, "A bidirectional DC-DC converter for an energy storage system with galvanic isolation," *IEEE Trans. Power Electron.*, vol. 22, no. 6, pp. 2299–2306, Nov. 2007.

[12] F. Krismer and J. W. Kolar, "Accurate power loss model derivation of a high-current dual active bridge converter for an automotive application," *IEEE Trans. Ind. Electron.*, vol. 57, no. 3, pp. 881–891, Mar. 2010.

[13] C. Yong-Won, C. Woo-Jun, K. Jung-Min, and K. Bong-Hwan, "High-efficiency bidirectional DAB inverter using a novel hybrid modulation for stand-alone power generating system with low input voltage," *IEEE Trans. Power Electron.*, vol. 31, no. 6, pp. 4138–4147, Jun. 2016.

[14] S. P. Engel, M. Stieneker, N. Soltau, S. Rabiee, H. Stagge, and R. W. De Doncker, "Comparison of the modular multilevel DC converter and the dual-active bridge converter for power conversion in HVDC and MVDC grids," *IEEE Trans. Power Electron.*, vol. 30, no. 1, pp. 124–137, Jan. 2015.

[15] R. W. A. A. D. Doncker, D. M. Divan, and M. H. Kheraluwala, "A three-phase soft-switched high-power-density DC/DC converter for high-power applications," *IEEE Trans. Ind. Appl.*, vol. 27, no. 1, pp. 63–73, Jan./Feb. 1991.

[16] Z. Biao, S. Qiang, L. Wenhua, and S. Yandong, "Overview of dual-active-bridge isolated bidirectional DC-DC converter for high-frequency-link power-conversion system," *IEEE Trans. Power Electron.*, vol. 29, no. 8, pp. 4091–4106, Aug. 2014.

[17] A. Rodriguez, A. Vazquez, D. G. Lamar, M. M. Hernando, and J. Sebastian, "Different purpose design strategies and techniques to improve the performance of a dual active bridge with phase-shift control," *IEEE Trans. Power Electron.*, vol. 30, no. 2, pp. 790–804, Feb. 2015.

[18] F. Bo, W. Yubin, and M. Jingbin, "A novel dual-phase-shift control strategy for dual-active-bridge DC-DC converter," in *Proc. 40th Annu. Conf. IEEE Ind. Electron. Soc.*, 2014, pp. 4140–4145.

[19] G. G. Oggier, G. O. Garcia, and A. R. Oliva, "Switching control strategy to minimize dual active bridge converter losses," *IEEE Trans. Power Electron.*, vol. 24, no. 7, pp. 1826–1838, Jul. 2009.

[20] G. G. Oggier, G. O. Garcia, and A. R. Oliva, "Modulation strategy to operate the dual active bridge DC-DC converter under soft switching in the whole operating range," *IEEE Trans. Power Electron.*, vol. 26, no. 4, pp. 1228–1236, Apr. 2011.

[21] D. Maksimovic, R. Zane, and R. Erickson, "Impact of digital control in power electronics," in *Proc. 16th Int. Symp. Power Semicond. Devices ICs*, 2004, pp. 13–22.

[22] M. Di Bernardo and F. Vasca, "Discrete-time maps for the analysis of bifurcations and chaos in DC/DC converters," *IEEE Trans. Circuits Syst. I, Fundam. Theory Appl.*, vol. 47, no. 2, pp. 130–143, Feb. 2000.

[23] G. C. Verghese, M. E. Elbuluk, and J. G. Kassakian, "A general approach to sampled-data modeling for power electronic circuits," *IEEE Trans. Power Electron.*, vol. PE-1, no. 2, pp. 76–89, Apr. 1986.

[24] B. Hua, M. Chunting, W. Chongwu, and S. Gargies, "The dynamic model and hybrid phase-shift control of a dual-active-bridge converter," in *Proc. 34th Annu. Conf. IEEE Ind. Electron.*, 2008, pp. 2840–2845.

[25] J. Guacaneme1, G. Garcerá1, E. Figueres1, I. Patrao1, and R. González-Medina1, "Dynamic modeling of a dual active bridge DC to DC converter with average current control and load-current feed-forward," *Int. J. Circuit Theory Appl.*, vol. 43, pp. 1311–1332, 2012.

[26] K. Zhang, Z. Shan, and J. Jatskevich, "Large- and small-signal average value modeling of dual-active-bridge DC-DC converter considering power losses," *IEEE Trans. Power Electron.*, vol. 32, no. 3, pp. 1964–1974, Mar. 2017.

[27] Q. Hengsi and J. W. Kimball, "Generalized average modeling of dual active bridge DC-DC converter," *IEEE Trans. Power Electron.*, vol. 27, no. 4, pp. 2078–2084, Apr. 2012.

[28] C. Zhao, S. D. Round, and J. W. Kolar, "Full-order averaging modelling of zero-voltage-switching phase-shift bidirectional DC-DC converters," *IET Power Electron.*, vol. 3, pp. 400–410, 2010.

[29] D. Costinett, R. Zane, and D. Maksimovic, "Discrete-time small-signal modeling of a 1 MHz efficiency-optimized dual active bridge converter with varying load," in *Proc. 2012 IEEE 13th Workshop Control Model. Power Electron.*, 2012, pp. 1–7.

[30] D. Costinett, "Reduced order discrete time modeling of ZVS transition dynamics in the dual active bridge converter," in *Proc. 2015 IEEE Appl. Power Electron. Conf. Expo.*, 2015, pp. 365–370.
[31] D. Costinett, R. Zane, and D. Maksimovic, "Discrete time modeling of output disturbances in the dual active bridge converter," in *Proc. 2014 29th Annu. IEEE Appl. Power Electron. Conf. Expo.*, 2014, pp. 1171–1177.
[32] S. Ling, L. Wanjun, J. Huang, L. Zhuoqiang, Y. Cui, and W. Yue, "Full discrete-time modeling and stability analysis of the digital controlled dual active bridge converter," in *Proc. 2016 IEEE 8th Int. Power Electron. Motion Control Conf.*, 2016, pp. 3813–3817.
[33] V. Rajasekaran, S. Jian, and B. S. Heck, "Bilinear discrete-time modeling for enhanced stability prediction and digital control design," *IEEE Trans. Power Electron.*, vol. 18, no. 1, pp. 381–389, Jan. 2003.
[34] S. Inoue and H. Akagi, "A bidirectional isolated DC-DC converter as a core circuit of the next-generation medium-voltage power conversion system," *IEEE Trans. Power Electron.*, vol. 22, no. 2, pp. 535–542, Mar. 2007.
[35] A. El Aroudi, L. Benadero, E. Toribio, and G. Olivar, "HOPF bifurcation and chaos from torus breakdown in a PWM voltage-controlled DC-DC boost converter," *IEEE Trans. Circuits Syst. I, Fundam. Theory Appl.*, vol. 46, no. 11, pp. 1374–1382, Nov. 1999.

Ling Shi received the B.S. degree from Xidian University, Xi'an, China, in 2014. She is currently working toward the M.S. degree in the State Key Laboratory of Electrical Insulation and Power Equipment, School of Electrical Engineering, Xi'an Jiaotong University, Xi'an.

Her research interests include modeling and control of dc–dc converters.

Wanjun Lei (M'07) received the B.S., M.S., and Ph.D. degrees in electrical engineering from Xi'an Jiaotong University, Xi'an, China, in 2000, 2004, and 2008, respectively.

He is currently an Assistant Professor with the School of Electrical Engineering, Xi'an Jiaotong University. His research interests include active power filters, power electronics inverters, reactive power compensation, and power quality control techniques.

Dr. Lei is a member of the China Power Supply Society.

Zhuoqiang Li received the B.S. degree in electrical engineering from Xi'an Jiaotong University, Xi'an, China, in 2014, where he is currently working toward the M.S. degree at the State Key Laboratory of Electrical Insulation and Power Equipment, School of Electrical Engineering.

His research interests include bidirectional dc–dc converters.

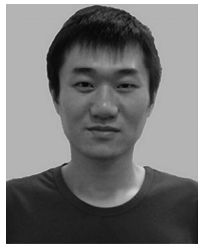

Jun Huang received the B.S. degree in electrical engineering from Xi'an Jiaotong University, Xi'an, China, in 2009, where he is currently working toward the Ph.D. degree at the State Key Laboratory of Electrical Insulation and Power Equipment, School of Electrical Engineering.

His research interests include high-frequency-link power conversion systems, isolated bidirectional dc–dc converters, and high-power IGBT drivers.

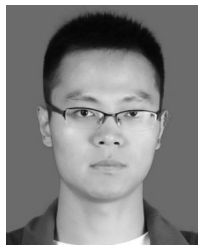

Yao Cui received the B.S. degree from Henan University of Science and Technology, Luoyang, China, in 2013. He is currently working toward the M.S. degree at the School of Electrical Engineering, Xi'an Jiaotong University, Xi'an.

His research interests include the control of cascaded dc dc converters.

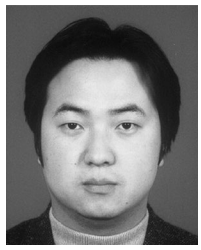

Yue Wang (M'05) received the B.S. and Ph.D. degrees from Xi'an Jiaotong University, China, in 1994 and 2004, respectively, and the M.S. degree from Beijing Jiaotong University, Beijing, China, in 2000, all in electrical engineering.

He is currently a Full Professor with the School of Electrical Engineering, Xi'an Jiaotong University. His research interests include active power filters, wind power generation, motor drives, multilevel converters, and high-voltage direct current.